# A two-dimensional computational study on the fluid–structure interaction cause of wing pitch changes in dipteran flapping flight

Daisuke Ishihara[1],*, T. Horie[1] and Mitsunori Denda[2]

[1]Kyushu Institute of Technology, 680-4 Kawazu, Iizuka, Fukuoka 8208502, Japan and [2]Rutgers University, 98 Brett Road, Piscataway, NJ 08854-8058, USA

*Author for correspondence (e-mail: ishihara@mse.kyutech.ac.jp)

## SUMMARY

**In this study, the passive pitching due to wing torsional flexibility and its lift generation in dipteran flight were investigated using (a) the non-linear finite element method for the fluid–structure interaction, which analyzes the precise motions of the passive pitching of the wing interacting with the surrounding fluid flow, (b) the fluid–structure interaction similarity law, which characterizes insect flight, (c) the lumped torsional flexibility model as a simplified dipteran wing, and (d) the analytical wing model, which explains the characteristics of the passive pitching motion in the simulation. Given sinusoidal flapping with a frequency below the natural frequency of the wing torsion, the resulting passive pitching in the steady state, under fluid damping, is approximately sinusoidal with the advanced phase shift. We demonstrate that the generated lift can support the weight of some Diptera.**

Key words: dipteran flight, dynamic similarity law, finite element method, fluid–structure interaction, wing torsional flexibility.

## INTRODUCTION

Flying insects depend on unsteady fluid dynamic effects to generate lift in their flapping flights. The majority of the experimental (Ellington et al., 1996; Dickinson et al., 1999; Usherwood and Ellington, 2002; Birch and Dickinson, 2003) and numerical (Liu et al., 1998; Wang, 2000; Sun and Tang, 2002; Rammamurti and Sandberg, 2002; Wang et al., 2004; Luo and Sun, 2005; Miller and Peskin, 2005) investigations have been performed with the rigid wing models that are given combined active flapping and pitching motions. These investigations have found that the unsteady fluid dynamic effects are significantly affected by the kinematical characteristics of the pitch motions such as the phase lag between pitching and flapping (Dickinson et al., 1999). On the other hand, many observations have reported the flexibility of the insect wings during flapping flights with various modes of deformation. The most significant among them is the high torsional flexibility in Diptera which is concentrated on the narrow wing basal and short root regions. The consequences of this are twofold: (1) it is hard to transmit the active torsion applied by the muscle to the outer wing and (2) the wing can twist easily to provide a passive change in the angle of attack (Ennos, 1987) or passive pitch motion.

In general, the passive pitch motion of the wings that solves the equation of motion balances three forces: wing inertial, elastic and fluid forces. According to Ennos (Ennos, 1988b), the wing inertial force accounts for much of the wing rotation at the stroke reversals in dipteran flapping flight. Although the wing inertial force might be dominant at the stroke reversals, where the acceleration is large, it is not enough to explain the passive pitch motion during the parts of the stroke other than the wing reversals. Investigation of the passive pitch motion during the entire stroke should be performed by taking into account all three of these forces. From the view point of the fluid surrounding the wings, these forces exerted on the wings act back on the fluid, producing a cycle of interaction between the

fluid and the wings, termed the fluid–structure interaction (FSI), through the equilibrium on their interface.

The aim of this paper was to reveal the details of the passive pitch motion due to wing torsional flexibility and its effects on lift generation by using (a) the non-linear FSI finite element method to analyze the precise motion of the wing passive pitching and the surrounding fluid flow, (b) characterization of the insect flight using a FSI similarity law, (c) the lumped torsional flexibility model as a simplified dipteran wing and (d) the analytical wing model.

The finite element method (Ishihara and Yoshimura, 2005; Ishihara et al., 2008) was used to solve the motion of the wing model which undergoes active sinusoidal flapping motion and passive pitching in the two-dimensional fluid. The numerical simulations are guided by the FSI similarity law (D.I., M.D. and T.H., manuscript submitted), which was used to correctly incorporate data from the selected real insect, the crane fly *Tipula obsolete* (Ellington, 1984a; Ellington, 1984b), and the robotic fly (Wang et al., 2004) into our wing model. The lumped torsional flexibility model consists of a plate with unit extent in the *z*-direction and an attached spring. The former models the wing cross-section averaged over the wing span. The latter models the concentrated torsional flexibility of the wing and allows the wing to twist around its torsional axis. We also introduced the analytical wing model, a single degree of freedom mass–spring–dashpot system, to explain characteristics of the passive pitching motion in the simulation.

The passive pitching motion of our wing model simulates well the real insect's pitching motion. The model wing keeps the high attack angle during its translation and rotates at the stroke reversals. The resulting pitch angle is approximately equal to that of the selected insect, the crane fly. It is especially important that the model wing begins to twist before it changes its flapping direction. Such advanced pitch motion is necessary in order for the insect flight to increase the lift force (Dickinson et al., 1999)

and is widely observed in insect flight. The analytical wing model explains the advanced pitch motion of the passive pitching as well as the torsion wave observed in the dipteran wing (Ennos, 1988b). The lift force generated by such passive pitching almost meets the force required to support the weight of the crane fly, but it is not quite enough. This could be attributed to the loosely attached leading edge vortex on the wing due to the long wing chord travel of the crane fly for the two-dimensional simulation. Indeed the lift of the fictitious insect flight, whose Reynolds number and stroke–wing chord ratio are much closer to those of the fruit fly model (Wang et al., 2004), shows a 35% increase compared with that of the crane fly flight due to the more tightly attached leading edge vortex on the wing.

## MATERIALS AND METHODS
### Non-linear finite element FSI analysis

To analyze wing motion, the surrounding fluid motion and their interaction, we used the finite element FSI analysis method (Ishihara and Yoshimura, 2005; Ishihara et al., 2008) based on the monolithic algorithm (Zhang and Hisada, 2001; Rugonyi and Bathe, 2001), which simultaneously solves the following equations.

(a) Navier–Stokes equations for the incompressible viscous fluid:

$$\rho^f \frac{\partial v_i^f}{\partial t} + \rho^f v_j^f \frac{\partial v_i^f}{\partial x_j} = \frac{\partial \sigma_{ji}^f}{\partial x_j} \tag{1a}$$

and

$$\frac{\partial v_i^f}{\partial x_i} = 0 , \tag{1b}$$

where $\rho$, $v_i$ and $\sigma_{ij}$ are the mass density, velocity and stress with the superscript f indicating the fluid. The fluid is assumed to be Newtonian. The stress $\sigma_{ij}^f = p\delta_{ij} + \mu(\partial v_i/\partial x_j + \partial v_j/\partial x_i)$ is used, where $\delta_{ij}$ is the Kronecker delta, $\mu$ is the fluid viscosity and $p$ is the fluid pressure. Body forces acting on the fluid are ignored for simplicity.

(b) Equation of motion for the elastic body:

$$\rho^s \frac{dv_i^s}{dt} = \frac{\partial \sigma_{ji}^s}{\partial x_j} , \tag{2}$$

where the superscript s refers to the structural quantity. We ignore the body forces acting on the elastic body. Let us consider the equation of motion of a flapping insect wing. Assuming that the insect is hovering perfectly, the net upward aerodynamic force acting on the wing will be equal in magnitude and opposite in direction to the gravitational force on the insect. Note that the wing weight is 2–4% of the body weight in the crane fly according to Ellington (Ellington, 1984a), whose data are used in this study. Thus the gravitational force on the wing can be ignored and the body force term is dropped in Eqn 2 describing the wing motion. In this study, the second Piola–Kirchhoff stress and the Green–Lagrange strain tensors are used. The latter is defined by $e_{ij}^s = 1/2[\partial u_i/\partial x_j + \partial u_j/\partial x_i + (\partial u_k/\partial x_i)(\partial u_k/\partial x_j)]$. We assume that the increments of these tensors are related by Hooke's law and the material non-linearity observed in biomaterials is ignored. This assumption is justified by the torsional test for the dipteran wing by Ennos (Ennos, 1988a). The test result for the wing without immobilization of its basal and root regions has shown that the relationship between the applied torque and the resulting angular displacement is approximately linear in pronation or supination.

(c) Geometrical compatibility and equilibrium conditions on the fluid–structure interface:

$$v_i^f = v_i^s , \tag{3a}$$

$$\sigma_{ij}^f n_j^f + \sigma_{ij}^s n_j^s = 0 , \tag{3b}$$

where $n_i^f$ and $n_i^s$ denote the outward unit normal vectors to the fluid and structure, respectively.

The arbitrary Lagrangian–Eulerian (ALE) method (Hughes et al., 1981) is used in order to take into account the deformable fluid–structure interface. For the elastic body, the total Lagrangian formulation is used in order to take into account the geometrical non-linearity due to the large deformation. The finite elements used for the fluid are the stabilized continuous linear velocity and pressure elements (Tezduyar et al., 1992), while those for the elastic plate are the mixed interpolation of the tensor component elements (Bathe and Dvorkin, 1985; Noguchi and Hisada, 1993). The details of the algorithm of the FSI method used in this study as well as its verification for the basic FSI problems are given by Ishihara and Yoshimura (Ishihara and Yoshimura, 2005).

We have selected the two-dimensional wing model similar to that used by Wang and colleagues (Wang et al., 2004) as a benchmark to test the validity of our method. Miller and Peskin (Miller and Peskin, 2005) have used a similar wing model to demonstrate the validity of their numerical technique. The wing is modeled by a thin rigid elastic plate of thickness $h$ with chord length $c$; in our elastic model a large Young's modulus is assigned to simulate the rigid body behavior. The model is two-dimensional having a unit extent in the $z$-direction (out-of-plane direction) without variation in this direction. Following Wang et al. (Wang et al., 2004), an $x$-displacement $U(t)$ and an angular displacement around the $z$-direction $a(t)$:

$$U(t) = \frac{A_0}{2} \cos 2\pi ft , \tag{4a}$$

$$a(t) = \beta \sin(2\pi ft + b) , \tag{4b}$$

are actively applied to the center of the wing, where $A_0$, $\beta$ and $b$ are the stroke amplitude, the amplitude of the pitching angle of attack and the phase shift, respectively. The common frequency $f$ of the flapping and pitching is set to produce the Reynolds number $Re = \rho^f V_{max} c/\mu = 75$, where $\rho^f$ is the fluid mass density, $\mu$ is the fluid viscosity and $V_{max} = \pi f A_0$ is the maximum wing velocity. The details of this test are described in the Appendix, where the time histories of force coefficients given by our method agree well with the results of Wang and colleagues (Wang et al., 2004).

### FSI similarity law

In this study, we introduced a dynamic similarity law for the FSI (D.I., M.D. and T.H., manuscript submitted) using the dimensional analysis of the equations of motion of the FSI system, Eqns 1a, 2 and 3b. Let $U$, $V$, $L$, $f$ and $P$ be the characteristic displacement, velocity, length, frequency and pressure, respectively. The similarity law consists of six non-dimensional numbers: $Re = \rho^f VL/\mu$ (the Reynolds number, the ratio between the inertial force due to the convective acceleration and the viscous force), $St = fL/V$ (the Strouhal number, the ratio between the inertial force due to the Eulerian time derivative acceleration and the inertial force due to the convective acceleration), $R_s = \rho^s L^2 f^2/E$ (the ratio between the inertial force due to the Lagrangian time derivative acceleration and the elastic force), $R_M = \rho^f/\rho^s$ (the mass number, the ratio between the fluid inertial force due to the Eulerian time derivative acceleration and the structural
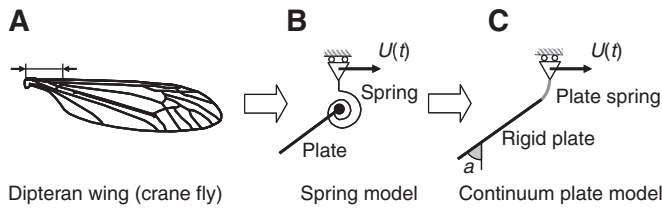
Fig. 1. Lumped torsional flexibility models. The original insect wing (A) with the arrows indicating the region of high torsional flexibility is drawn after Ennos (Ennos, 1988a). The spring model (B) shows the concept of the present lumped torsional flexibility model, and the continuum plate model (C) shows its computational implementation using the continuum plate. Note that the span-wise direction or the torsional axis is perpendicular to the plane in B and C. The pitching motion is evaluated using the angular displacement or pitch angle $a$, which is the slope angle of the trailing edge of the wing as shown in C. $U(t)$, $x$-displacement of the wing base.
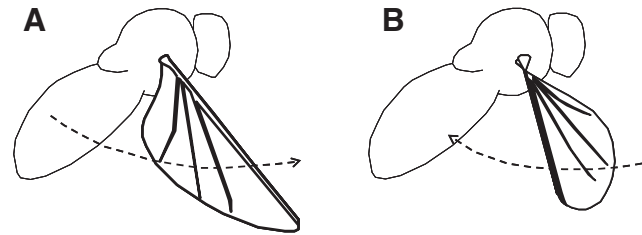


Fig. 2. Wing torsion during the downstrokes (A) and upstrokes (B) drawn after Ennos (Ennos, 1988a). Most of the wing torsional flexibility in Diptera is concentrated on the narrow basal and short root regions of the wings, and allows the wing to twist around its torsional axis in a span-wise direction.

inertial force due to the Lagrangian time derivative acceleration), $R_{Is}=f\mu/E$ (the ratio between the fluid viscous and elastic forces) and $R_{Ip}=\rho^f VLf/E$ (the ratio between the fluid dynamic pressure and the elastic force), where the characteristic pressure $P$ is evaluated by the magnitude of the dynamic pressure $\rho^f V^2$. Only four of them are independent due to the relationships $R_{Ip}/R_{Is}=Re$ and $R_M=R_s\times St\times R_{Ip}$. The numbers $R_s$, $R_{Is}$ and $R_{Ip}$ are new as far as we know.

Two systems that are geometrically similar are also dynamically similar if the non-dimensional numbers introduced above are equal. The FSI similarity law was verified through the numerical examples of (a) the forced vibration of an elastic cantilever plate in the quiescent fluid (the problem analyzed in this paper in the context of flapping flight), and (b) the flow-induced vibration of an elastic cantilever plate situated in the wake of a rectangular prism in the uniform flow (D.I., M.D. and T.H., manuscript submitted). In each example, five dynamically similar systems with different fluid and/or reference length were analyzed by our finite element FSI method. In order to verify the validity of the present law, all the governing equations were cast in the dimensional form deliberately. The dynamic similarity of these systems was successfully verified, with the relative error of the results being less than 1% in all cases.

In the dimensional analysis of the equations of the motion of the FSI system, we assumed the linear strain tensor $e^s_{ij}=1/2(\partial u_i/\partial x_j+\partial u_j/\partial x_i)$ and a linear relationship (Hooke's law) between the stress and strain tensors. We also used an alternative approach to the dimensional analysis of the general FSI system including, but not limited to, the linear elastic equation. We defined the following fundamental variables of the FSI system on which the system motion is dependent: $L$, $U$, $V$, $P$, $\rho^s$, $\rho^f$, $E$ (Young's modulus) and $\mu$. Applying the standard procedure of the dimensional analysis to these variables, we found the same non-dimensional numbers as before. The former analysis ensures that our law is the general framework of the dynamic similarity law. The latter analysis ensures that our law can be applied to the FSI system with large deformation of the elastic body.

The numerical simulations are guided by the FSI similarity law, which was used to correctly incorporate data from a selected real insect, the crane fly (Ellington, 1984a; Ellington, 1984b), and a robotic fly (Wang et al., 2004) into our wing model. It is very interesting how these parameters vary for a variety of flying insects and their flight performances change as each number is varied. In the numerical experiments of this study, comparison of the leading edge vortex behaviors between the crane fly and fictitious insect

flight deals to some extent with these questions. The leading edge vortex becomes more tightly attached to the wing as $Re$ and $St$ are decreased while $R_M$ and $R_{Is}$ are preserved. In future work, we will tackle these interesting questions.

## Lumped torsional flexibility model

Most of the wing torsional flexibility in Diptera is concentrated on the narrow basal and short root regions of the wings as shown in Fig. 1A, and allows the wing to twist around its torsional axis in a span-wise direction as shown in Fig. 2 (Ennos, 1987; Ennos, 1988a). Based on these facts, (1) we modeled the wing two-dimensionally by a rectangular plate, with chord length $c$ and a unit extent in the out-of-plane direction ($z$-direction), which is the span-wise average of the varying cross-section, and (2) we modeled the torsional flexibility of the wing as an elastic spring, i.e. the torsional flexibility of the wing is lumped into the spring and its torsional stiffness is characterized by the spring constant (the lumped torsional flexibility model). The concept of the lumped torsional flexibility model is shown in Fig. 1B. Initially, the wing is at rest with the angular displacement or pitch angle $a=0$ in the two-dimensional fluid and then the sinusoidal flapping motion in the $x$-direction (Eqn 4a) is applied at its leading edge, where it is supported by a roller. The flapping motion is approximated by the sinusoidal function in this study because the actual kinematics of flies and bees are similar to this simple motion (Ellington, 1984b). We used a continuum plate model as shown in Fig. 1C. This is because the plate spring is easily discretized by using finite elements. This model consists of two parts: the upper narrow part of length $l_s$ and the rest with low and high bending rigidities to simulate the spring (s) and the rigid body (r), respectively. The thickness and Young's modulus of the former are $h_s$ and $E_s$ and those for the latter are $h_r$ and infinity, respectively. The infinite Young's modulus is approximated by setting a value far larger than $E_s$. The mass density is set to a uniform value $\rho^s$ over the
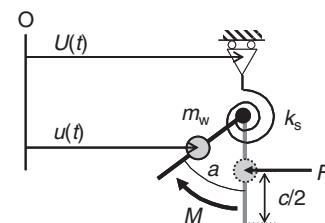


Fig. 3. A single degree of freedom mass–spring–dashpot system of the wing. $U(t)$ and $u(t)$, $x$-displacement of the wing base and center, respectively; $m_w$, wing mass; $k_s$, spring constant; $F$, force; $c$, chord length; $M$, moment.

entire plate. Few data concerning the wing torsional flexibility are available. Ennos (Ennos, 1988a) has investigated the wing torsional stiffness of some Diptera such as crane, drone and blow flies. The Reynolds number of crane fly flight ($Re \approx 290$) is near to that of the robotic fly flight ($Re \approx 100$) (Wang et al., 2004), while the Reynolds numbers of the flights of drone and blow flies are over 1000. We selected the crane fly in this study because the applicability of our numerical method to the flapping wing has been verified in the flow regime of low Reynolds number using the robotic fly data (see Appendix). The high torsional flexibility region around the wing base of the crane fly is schematically denoted by the arrows in Fig. 1A. The chord length of this region is approximately 10–30% of the maximum chord length that occurs at mid-span. Since the upper narrow part of the continuum plate model corresponds to the high torsional flexibility region, we define the length $l_s$ of the continuum plate model as $0.2c$. Under this setting, we obtain the following non-dimensional numbers in the FSI similarity law.

Dynamic numbers:

$$St = \frac{fc}{V_{max}} = \frac{c}{\pi A_0} , \tag{5a}$$

$$Re = \frac{\rho^f V_{max} c}{\mu} , \tag{5b}$$

$$R_{Is} = \frac{f \mu}{E_s} , \tag{5c}$$

$$R_M = \frac{\rho^f}{\rho^s} , \tag{5d}$$

Geometric numbers:

$$\gamma_r = \frac{c}{h_r} , \tag{6a}$$

$$\gamma_s = \frac{c}{h_s} . \tag{6b}$$

The parameters of the continuum plate model are determined so that the non-dimensional numbers (Eqns 5 and 6) agree with those for the real insect. The real insect selected was the crane fly (Ellington, 1984a; Ellington, 1984b), with span length of one wing $R=1.27$ cm, total area of the wing pair $S=0.59$ cm$^2$, stroke angle $\varphi=123$ deg., flapping frequency $f=45.5$ Hz and mass of the wing pair $m_w=0.000245$ g. The total mass of the insect is $m=0.0114$ g. The averaged chord length $c$ is given by $S/(2R)=0.23$ cm. Let $\rho^s=1.2$ g cm$^{-3}$ be the wing mass density (Jensen and Weis-Fogh, 1962; Wainwright et al., 1982); the averaged thickness is then $h=m_w/(\rho^s S)=0.00069$ cm, which is identified as the thickness $h_r$ of the hypothetical rigid part of the real insect. The stroke amplitude $A_0$ of this flapping is estimated by the arc length traveled by the chord at the mid-span and is given by $0.5R(\varphi/180)\pi=1.36$ cm. The value of the Young's modulus $E_s$ is 6.1 GPa (Wainwright et al., 1982) and those for the fluid mass density $\rho^f$ and viscosity $\mu$ are $\rho^f=0.0012$ g cm$^{-3}$ (air) and $\mu=0.00018$ g (cm s)$^{-1}$ (air), respectively. The non-dimensional numbers $St$, $Re$, $R_{Is}$, $R_M$ and $\gamma_r$ are determined to be 0.054, 290, $1.4\times10^{-13}$, $1.0\times10^{-3}$ and 340, respectively, using the above properties. On the other hand, the number $\gamma_s$ is determined based on the expectation that it is of the same order as $\gamma_r$; among the numerically tested values of $\gamma_s$ in the region of $\gamma_r=340$, we have found that $\gamma_s=900$ maximizes the averaged lift. To test the validity of this selection of $\gamma_s=900$, consider the bending of the continuum plate spring with its upper end fixed and the moment $M$ applied at the lower end. The slope of the plate at its lower end, using the Euler–Bernoulli beam
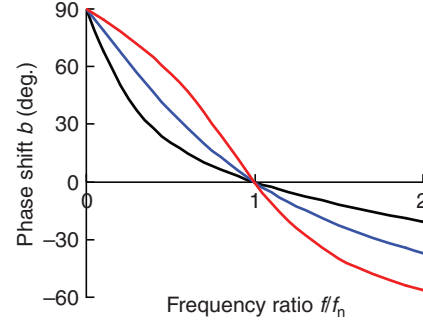


Fig. 4. The relationship between the frequency ratio $f/f_n$ and the phase shift $b$ for the damping ratios $\zeta=0.5$ (red line), 1 (blue line) and 2 (black line).
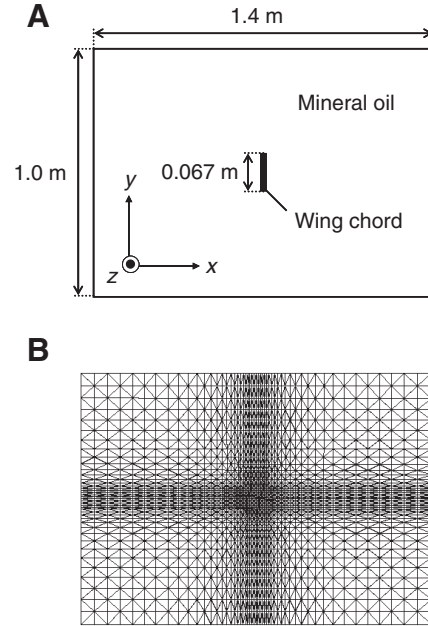


Fig. 5. (A) Schematic view of the analysis domain, and (B) the finite element mesh. A unit length in the $z$-direction is assumed.

assumption, is given by $a=Ml_s/(E_sI)$, where $I=h_s^3/12$ is the second moment of area for the plate spring. Thus the spring constant of the plate is given by $k_s=E_sI/l_s=E_sh_s^3/(12l_s)$, which is set to the macroscopic torsional stiffness $G_w$ of the insect wing. Notice that the selected value of $\gamma_s=c/h_s=900$ gives $k_s=1.9$ g cm$^2$(s$^2$ rad)$^{-1}$, which lies in the range of values for $G_w=0.8$–15.4 g cm$^2$(s$^2$ rad)$^{-1}$ (Ennos, 1988a) obtained for the crane fly.

The torsional axis of our model is located within the upper 20% of the wing chord and that of the real insect is located near the leading edge. We investigate the effects of the location of the rotational axis in the Appendix, where we show that they can be neglected with slight perturbation in the force amplitude and phase shift.

**Analytical wing model**

In order to explain the characteristics of the passive pitching of the continuum plate model, we introduced a single degree of freedom mass–spring–dashpot system of the wing (Fig. 3) for the theoretical analysis. The wing is modeled by a rigid rod of length $c$ and its angular displacement $a(t)$ is assumed to be small enough that it can be measured by the relative $x$-displacement $\delta(t)=u(t)-U(t)$ of the wing center according to $a(t)=\delta(t)/(c/2)$ (assumption of linearization),

where $U(t)$ and $u(t)$ are the displacement of the wing base and center, respectively. We assume that the wing mass is concentrated on the wing center and, to be consistent with the scheme of linearization, the resultant force on the wing is assumed to act on the wing center in the $x$-direction.

The linearized motion of the concentrated wing mass is given by:

$$m_w d^2 u \,/\, dt^2 + c_f d\delta(t) \,/\, dt + k_s' \delta(t) = 0 \,, \qquad (7)$$

where the first, second and third terms represent the wing inertial force $f_i = m_w d^2 u / dt^2$, the fluid damping force $f_c = c_f (du/dt - dU/dt) = c_f d\delta(t)/dt$ and the restoring force $f_s = k_s'[u(t) - U(t)] = k_s' \delta(t)$ due to the spring. The coefficient $k_s'$ is the spring constant for the relative $x$-displacement $\delta(t) = u(t) - U(t)$ and is obtained by linearizing the moment and angular displacement relationship $M = k_s a$ according to $a = \delta/(c/2)$ and $M = f_s(c/2)$, with the result $f_s = k_s' \delta$, where:

$$k_s' = 4 k_s / c^2 \,. \qquad (8)$$

In addition, $c_f$ is the damping force coefficient due to the fluid and the subtraction $dU/dt$ is the fluid advection effect induced by the wing global flapping motion.

This equation of motion is reduced to the following equation:

$$m_w \frac{d^2 \delta}{dt^2} + c_f \frac{d\delta}{dt} + k_s' \delta = F_0 \cos 2\pi f t \,, \qquad (9)$$

where $F_0 = m_w U_0 (2\pi f)^2$ is the amplitude of the periodic exciting force $F_0$ given in terms of the amplitude $U_0$ ($=A_0/2$) and the frequency $f$ of the spring base displacement $U(t)$ given by Eqn 4a. The analytical solution of Eqn 9 in the steady state is given by:

$$\delta(t) = \kappa \delta_0 \sin(2\pi f t + b) \,, \qquad (10)$$

with:

$$\delta_0 = \frac{F_0}{k} = \frac{m_w A_0 (2\pi f)^2}{2k} \,, \qquad (11a)$$

$$\kappa = \frac{1}{\sqrt{[1 - (f / f_n)^2]^2 + [2\zeta(f / f_n)]^2}} \,, \qquad (11b)$$

$$b = \frac{\pi}{2} - \tan^{-1} \frac{2\zeta(f / f_n)}{1 - (f / f_n)^2} \,, \qquad (11c)$$

where

$$f_n = \sqrt{k_s' / m_w} \,/\, 2\pi \qquad (12)$$

and

$$\zeta = c_f / (2\sqrt{m_w k_s'}) \,, \qquad (13)$$

are the natural frequency and the damping ratio, respectively.

Fig. 4 shows the dependence of the phase shift $b$ on the frequency ratio $f/f_n$ for three representative values of the damping ratios $\zeta = 0.5$ (under damping), 1 (critical damping) and 2 (over damping). Regardless of the value of $\zeta$, the phase shift $b$ is (a) positive (advanced phase shift) for $f/f_n < 1$, (b) zero (no phase shift) for $f/f_n = 1$



Fig. 6. Time histories of the lift ($C_L$, A) and drag ($C_D$, B) coefficients for the wing motion of the flexible wing with the passive pitching (black line) and the wing motion of the rigid wing using this passive pitching as the active one (red line).
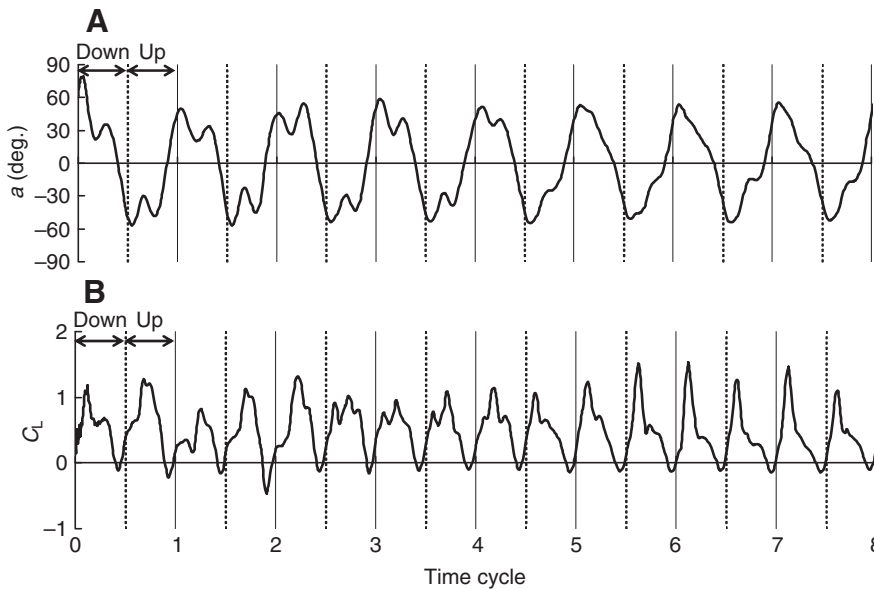


Fig. 7. Time histories of the simulated passive pitching motion (A) and the normalized lift coefficient $C_L$ generated by it (B). The pitching motion is evaluated using the angular displacement or pitch angle $a$, which is the slope angle of the trailing edge of the wing. The vertical lines and the attached arrows show the range of each half-stroke for the downstroke (Down) and upstroke (Up).
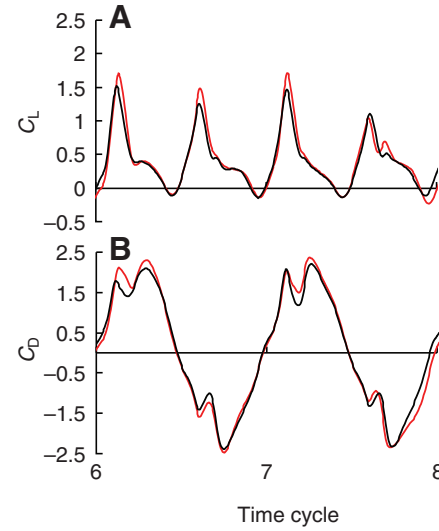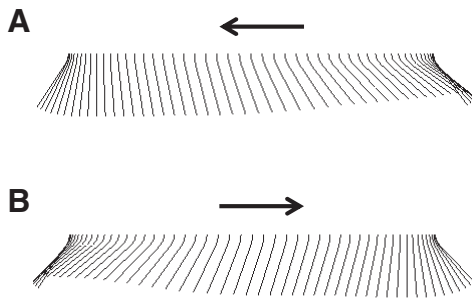
**A**

**B**

Fig. 8. The frame-by-frame advance of the wing motion from 7 to 8 cycles. The time interval between each frame is 0.01 cycles. The wing chord moves from right to left in the downstroke 7 to 7.5 cycles (A) and left to right in the upstroke 7.5 to 8 cycles (B). The arrows indicate the flapping direction.

and (c) negative (delayed phase shift) for $f/f_n>1$, respectively. Note that the amount of the advanced phase shift increases as the value of $f/f_n$ (<1) gets smaller.

## RESULTS AND DISCUSSION

Once the chord length $c$ and the fluid material properties $\rho^f$ and $\mu$ are specified in our continuum plate model, all the other properties, the flapping frequency $f$, stroke amplitude $A_0$, plate thicknesses $h_r$ and $h_s$, plate material properties $\rho^s$ and $E_s$, are determined to match the non-dimensional numbers of the FSI similarity law $Re$, $St$, $R_M$, $R_{Is}$, $\gamma_r$ and $\gamma_s$ obtained from the real insect. We used $c=6.7$ cm and the material properties of mineral oil $\rho^f=0.88$ g cm$^{-3}$ and $\mu=0.715$ g (cm s)$^{-1}$ in the scaled computation, following the dynamically scaled model of Dickinson and colleagues (Dickinson et al., 1999). Since our plate is flexible at the upper narrow part, unlike the rigid wing model of Dickinson and colleagues (Dickinson et al., 1999), not only the fluid motion but also the plate motion and their interaction are dynamically scaled to the real insect flapping flight. Fig. 5 shows the schematic view of the analysis domain and the finite element mesh employed, in which the no-slip condition is assumed on the outer boundary of the fluid domain and the wing chord. A convergence test where the fluid grid is refined is provided in the Appendix. The center of the wing is located at the center of the fluid domain initially. We first apply the
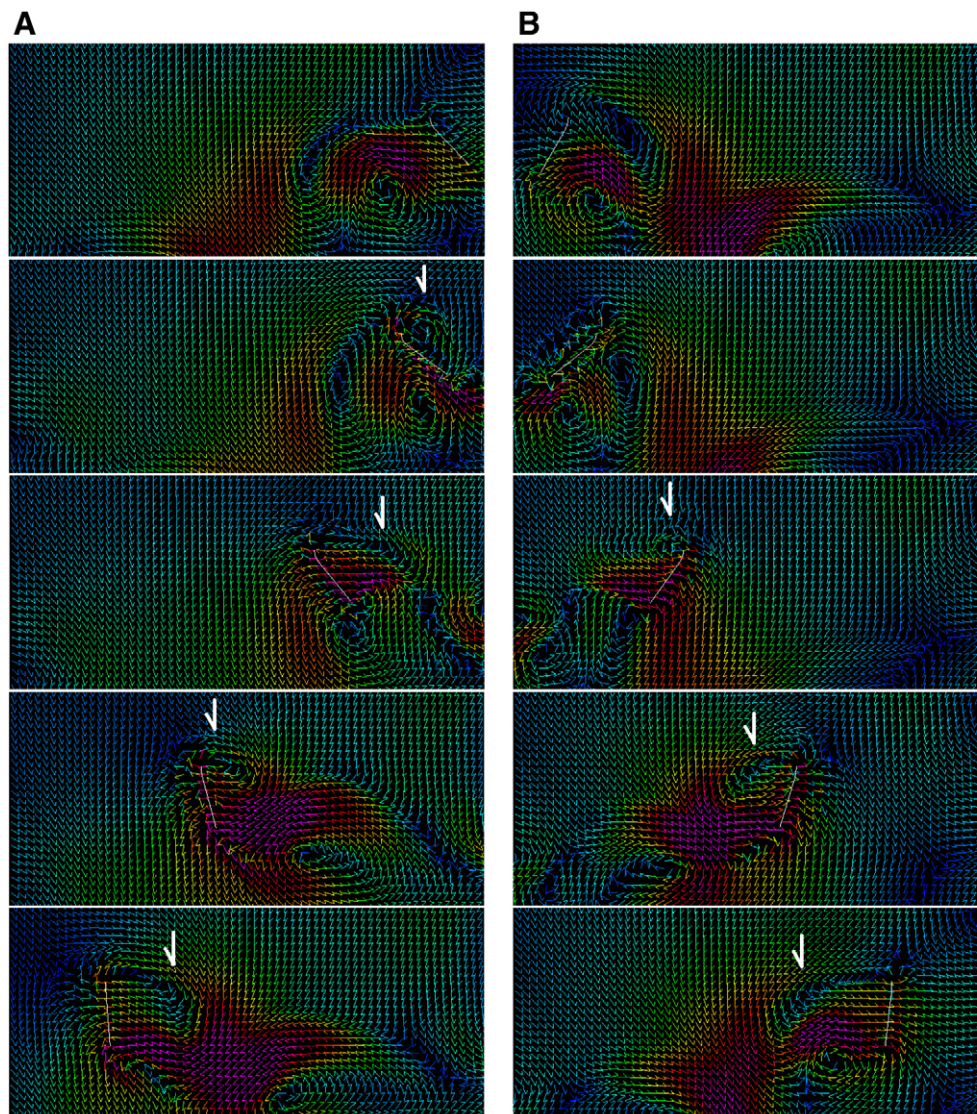


**A**

**B**

Fig. 9. Fluid velocity fields from 7 to 7.9 time cycles for the crane fly (Reynolds number $Re=290$, Strouhal number $St=0.054$, corresponding to $A_0/c=5.9$, where $A_0$ is stroke amplitude). The time interval between each snapshot is 0.1 cycles. The arrows point in the direction of fluid velocity with their color indicating the magnitude; pink and blue correspond to $V_{max}=35$ cm s$^{-1}$ and 0, respectively. The wing chord is represented by the white line. Columns A and B represent the downstroke (from 7 to 7.4 cycles) and the upstroke (from 7.5 to 7.9 cycles), respectively. The wing moves from right to left during the downstroke and from left to right during the upstroke. The white arrows indicate the positions of the leading edge vortices. The figures in the left column show that the leading edge vortex was detached from the wing at the middle of the downstroke and then reproduced. The figures in the right column show that the leading edge vortex was loosely attached to the wing.
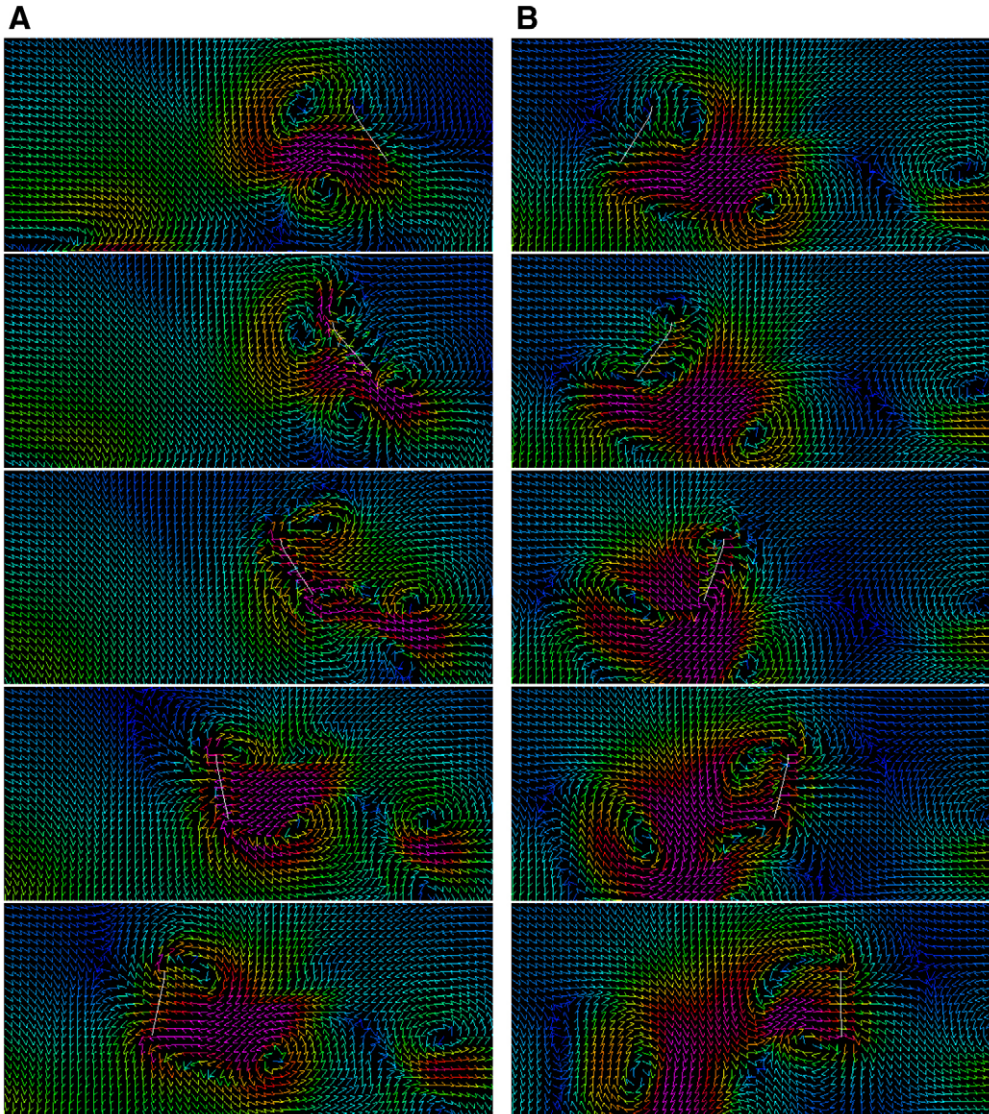
**A**

**B**



Fig. 10. Fluid velocity fields from 4 to 4.9 time cycles for the fictitious insect ($Re$=200, $St$=0.1 corresponding to $A_0/c$=3.2). The time interval between each snapshot is 0.1 cycles. The arrows point in the direction of the fluid velocity with their color indicating the magnitude; pink and blue correspond to $V_{max}$=24 cm s$^{-1}$ and 0, respectively. The wing chord is represented by the white line. Columns A and B represent the downstroke (from 4 to 4.4 cycles) and the upstroke (from 4.5 to 4.9 cycles), respectively. The wing moves from right to left during the downstroke and from left to right during the upstroke.

sinusoidal flapping motion Eqn 4a in the $x$-direction at the leading edge of the flexible wing to measure the induced passive pitching in terms of the angular displacement or pitch angle $a(t)$ of the trailing edge of the wing. The angular displacement $a(t)$ is measured from the rest position of the wing as shown in Fig. 1C. The anti-clockwise direction is positive. Note that no angular displacement $a(t)$ is applied actively. Next, we consider a rigid wing model and apply both the sinusoidal flapping motion Eqn 4a and the measured angular displacement $a(t)$ actively to calculate the fluid forces. As shown in Fig. 6, the fluid forces obtained in the two cases are in fine agreement. Since the ability of our method to simulate the two-dimensional wing motion under the combined active flapping and pitching for the rigid wing has been verified in the Appendix, this agreement serves as a benchmark to validate our method for the flexible wing that induces passive pitching under active flapping.

### Passive pitching motion

Figs 7 and 8 summarize the passive pitching motion of our continuum plate model wing. Fig. 7 also shows the generated lift history. After the initial transient phase, the angular displacement or pitch angle $a$ oscillates regularly after around four cycles as shown in Fig. 7. The initial transient phase can be explained by the equation of motion (Eqn 9) of the analytical wing model. The analytical solution of Eqn 9 consists of the free and forced vibration modes initially. However, the free vibration mode disappears due to the damping effect after multiple strokes and the forced vibration mode remains. Note that the analytical solution of the forced vibration mode is given by Eqn 10. The same phenomenon occurs in the pitching motion of the continuum plate model wing. Following the stabilization of the wing motion, the lift coefficient also oscillates regularly.

The passive pitching motion shown in Fig. 8 seems to simulate well the real insect's pitching motion. The model wing keeps the high attack angle during its translation and rotates at the stroke reversals. In addition, our wing model gives a maximum pitch angle of 50–60 deg., which lies in the range of values for the crane fly, 45–65 deg. (Ellington, 1984b). Note that the pitch angle is a non-dimensional variable. It is especially important that the model wing begins to twist before it changes its flapping direction as shown in Figs 7 and 8. Such advanced pitch motion is important for the insect flight to increase the lift force by intercepting the wake of the previous stroke (wake capture) (Dickinson et al., 1999) and is widely observed in insect flight.
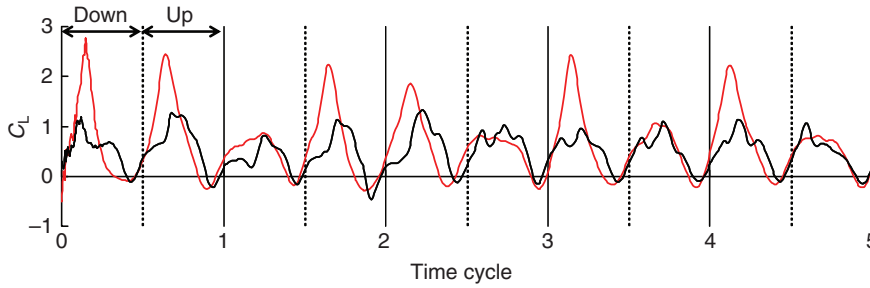
Fig. 11. Time histories of the lift coefficient $C_L$ for the fictitious insect (red line) and the crane fly (black line). Note that both traces show simulations (not experimental data), and that in the fictitious insect case the leading edge vortex does not separate because of the short length of translation. The vertical lines and the attached arrows show the range of each half-stroke for the downstroke (Down) and upstroke (Up).

The advanced pitch motion observed in Figs 7 and 8 can be explained by the analytical wing model as follows. The time history of the pitch angle $a(t)$ takes a form similar to a sinusoidal function with the same frequency $f$ as flapping in the regular oscillation after around four cycles. Thus, the time history of pitching in the steady state is approximately expressed by Eqn 4b with the positive phase shift $b$. The fact that our analytical model, excited by the sinusoidal force in Eqn 9 and subject to damping, attains the sinusoidal oscillation (Eqn 10) for the relative displacement $\delta(t)=ca(t)/2$ in the steady state provides convincing support for the presence of the sinusoidal passive pitching $a(t)$ in our continuum plate model. As shown in Fig. 4, regardless of the value of $\zeta$, the phase shift $b$ is (a) positive (advanced phase shift) for $f/f_n<1$, (b) zero (no phase shift) for $f/f_n=1$ and (c) negative (delayed phase shift) for $f/f_n>1$, respectively. For our model wing the spring constant $k_s'$, given by Eqn 8 with $k_s=1.9\,\mathrm{g\,cm^2\,(s^2\,rad)^{-1}}$ and $c=0.23\mathrm{cm}$, is equal to $144\,\mathrm{g\,s^{-2}}$, while the wing mass $m_w=\rho^s c(0.2h_s+0.8h)=0.000166\mathrm{g}$. Thus the natural frequency calculated by Eqn 12 is $f_n=148\mathrm{Hz}$ which gives the ratio $f/f_n=0.31<1$, where $f=45.5\mathrm{Hz}$. This shows that our continuum plate model wing satisfies the condition $f/f_n<1$ for advanced pitching.

The analytical wing model also provides an insight into the tip to base torsion wave observed in dipteran flight (Ennos, 1988b). As shown in Fig. 4, the value of the advanced phase shift $b$ increases as the value of $f/f_n$ (<1) gets smaller. Since the natural frequency $f_n$ given by Eqn 12 increases when the wing mass $m_w$ is reduced, the phase shift is bigger for the lighter wing mass. Consequently, when we move from the base to the tip of the wing, the wing mass becomes lighter (Ennos, 1989) and the phase shift becomes larger. Such a phase shift gradient along the span-wise direction appears as the torsion wave in the three-dimensional wing. We need to be careful, however, with the limitations of our continuum plate model of the wing for which the chord length is obtained as an average over the span-wise direction and the motion represented is an average over the span. Nevertheless, our simple analytical model provides an insight into the tip to base torsion wave observed in dipteran flight (Ennos, 1988b).

**Lift generated by wing motion including passive pitching**
We found that the lift force generated by passive pitching almost meets the required force to support the weight of the crane fly. Fig. 7B shows the time history of the lift coefficient $C_L$ (normalized by $0.5\rho^f cV_{max}^2$) in the wing motion with passive pitching. Its mean value $C_{L,mean}=0.46$ gives the mean combined lift force $f_{L,mean}=6.8\times10^{-5}\mathrm{N}$ for both wings of the crane fly, which is comparable to but smaller than the weight of the crane fly $w=11\times10^{-5}\mathrm{N}$. This could be attributed to the loosely attached leading edge vortex on the wing due to the long wing chord travel of the crane fly for the two-dimensional simulation. In the two-dimensional simulation with $Re=75$–$115$ and the stroke–wing chord ratio $A_0/c=2.8$–$4.8$ for the fruit fly, the wing reverses before the leading edge vortex has time to separate during each stroke. Thus in these cases the additional

mechanism is not required to stabilize the leading edge vortex and the lift generated provides a good approximation of the corresponding lift in the three-dimensional experiment (Wang et al., 2004). In our two-dimensional simulation with $Re=290$ and $A_0/c=5.9$ ($St=0.054$) for the crane fly, the leading edge vortex appears to be slightly separated from the wing as shown in Fig. 9. Due to the larger wing travel length or the larger stroke–wing chord ratio and the smaller Strouhal number than those of Wang and colleagues (Wang et al., 2004), the leading edge vortex separates from the wing before the wing reverses in our two-dimensional simulation with no additional stabilization mechanism such as the span-wise flow effect. If we adopt a fictitious insect with $Re=200$ and $A_0/c=3.2$ ($St=0.1$), whose characteristics are closer to those of the model of Wang and colleagues (Wang et al., 2004) than to those of the crane fly, the leading edge vortex is more tightly attached to the wing as shown in Fig. 10. Consequently, the lift coefficient of the fictitious insect is higher than that of the crane fly as shown in Fig. 11 with an approximately 35% increase in the mean lift coefficient ($C_{L,mean}=0.62$) compared with that of the crane fly. Pitching in this case is also advanced, as in the case of the crane fly.

It is important to remember here that it is hard to transmit the active torsion applied by the muscle to the outer wing due to the wing torsional flexibility in Diptera (Ennos, 1987), while the wing pitch is adequately controlled to produce the lift to enable the insect to hover. Our wing model meets these criteria and explains the mechanism of insect flight with passive pitching. It seems to be natural for insects to select such a passive mechanism to minimize the effort required to move their wings. This passive mechanism might be useful as the design principle for developing micro-air vehicles, i.e. engineers can avoid the need to develop the active mechanism to drive and control the wing pitch adequately.

## APPENDIX
### Testing the validity of our FSI analysis method
We have selected the two-dimensional wing model similar to that used by Wang and colleagues (Wang et al., 2004) as a benchmark
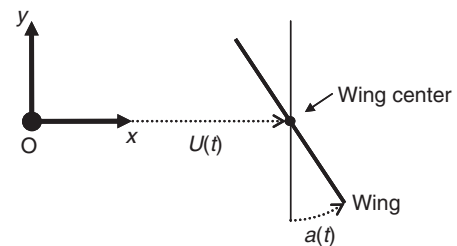


Fig. A1. The two-dimensional wing model similar to that used by Wang and colleagues (Wang et al., 2004) as a benchmark to test the capability of our method. The $x$-displacement $U(t)$ and an angular displacement around the $z$-direction $a(t)$ are actively applied to the wing center.
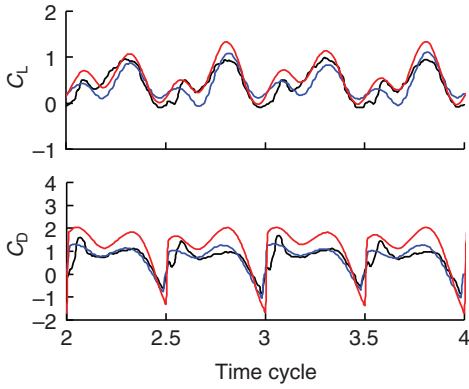
Fig. A2. Comparisons of the time histories of $C_L$ and $C_D$. The red and blue lines show the results given by the present method and that of Wang and colleagues (Wang et al., 2004), respectively, while the black line represents the experimental data given by Wang and colleagues (Wang et al., 2004).
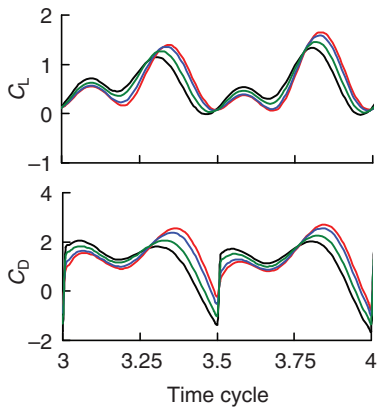


Fig. A3. Time histories of $C_L$ and $C_D$ for the different positions of the axis of rotation. The black, red, blue and green lines correspond to positions O (centre), A (top), B (upper 1/10) and C (upper 1/3), respectively.
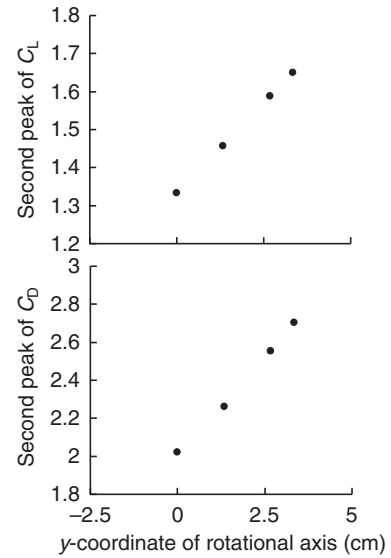


Fig. A4. The relationship between the rotational axis positions and the second peak values of the force coefficients from 3.5 to 4 cycles in Fig. A3.

to test the capability of our method. The wing is modeled by a thin rigid elastic plate of thickness $h$ with chord length $c$; in our elastic model a large Young's modulus is assigned to simulate the rigid body behavior. The model is two-dimensional having the unit extent in the $z$-direction (out-of-plane direction) without variation in this direction. Following Wang et al. (Wang et al., 2004), an $x$-displacement $U(t)$ and an angular displacement around the $z$-direction $a(t)$:

$$U(t) = \frac{A_0}{2}\cos 2\pi ft , \qquad (A1a)$$

$$a(t) = \beta \sin(2\pi ft + b) , \qquad (A1b)$$

are actively applied to the center of the wing as shown in Fig. A1, where $A_0=2.8c$, $\beta=\pi/4$ and $b=0$ are the stroke amplitude, the

amplitude of the pitching angle of attack and the phase shift, respectively. The common frequency $f$ of the flapping and pitching is set to produce the Reynolds number $Re=\rho^f V_{max}c/\mu=75$, where $\rho^f$ is the fluid mass density, $\mu$ is the fluid viscosity and $V_{max}=\pi fA_0$ is the maximum wing velocity. The wing starts its downstroke with the initial angular displacement $a(0)=a_0=0$. Notice that this wing motion agrees with that used by Wang and colleagues (Wang et al., 2004) with symmetrical pitching. Miller and Peskin (Miller and Peskin, 2005) have used a similar wing model with symmetrical pitching to demonstrate the validity of their numerical technique. Fig. A2 gives the time history of lift coefficient $C_L$ and drag coefficient $C_D$, normalized by $0.5\rho^f c V_{max}^2$, which shows very good agreement with the results of Wang and colleagues (Wang et al., 2004). As, in both simulations, the leading edge vortex is attached to the wing during the wing stroke, the lift coefficient agrees well with that obtained from the three-dimensional experiment even though the three-dimensional axial flow is absent.

In the benchmark problem described above, where comparison with the results of Wang and colleagues (Wang et al., 2004) was made, the position of the axis of rotation is located at the center of the wing. In contrast, the position of the rotational axis of our lumped flexibility model is located within the upper 20% of the wing, while that of the real insects is located near the leading edge. Thus the effects of the location of the axis of rotation need to be investigated. We applied $U(t)$ and $a(t)$ at four positions; center (O), top (A), upper 1/10 (B) and upper 1/3 (C). Fig. A3 shows the time history of $C_L$ and $C_D$ for these positions, and Fig. A4 shows the relationship between the rotational axis positions and the second peak value of the force coefficients from 3.5 to 4 cycles in Fig. A3. As shown in
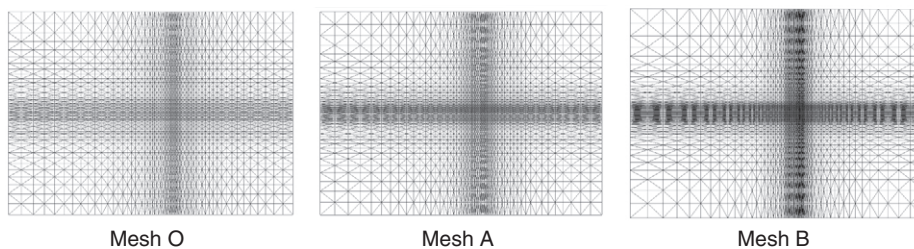


Mesh O          Mesh A          Mesh B

Fig. A5. Convergence test where the fluid grid is refined. Mesh O (the number of nodes and elements is 3417 and 6600, respectively) is used to give the results in Figs A2, A3 and A4. The refined meshes A (the number of nodes and elements is 3905 and 7560, respectively) and B (the number of nodes and elements is 4697 and 9120, respectively) have 1.4 and 2 times finer space resolutions, respectively, around the wing.
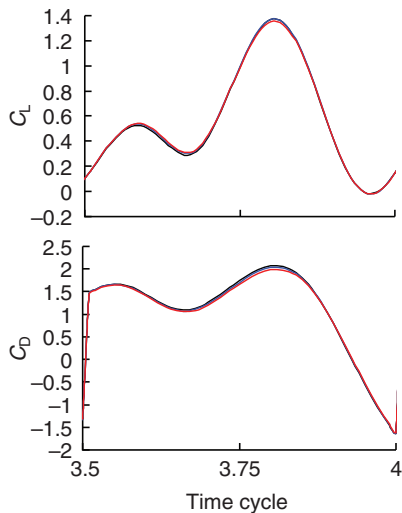
Fig. A6. Comparison of the time histories of $C_L$ and $C_D$. The black, blue and red lines show the results obtained using meshes O, A and B, respectively.

Fig. A3, the time histories of $C_L$ and $C_D$ for the four positions are similar. As shown in Fig. A4, the force coefficients vary linearly. $C_L$ varies from 1.46 to 1.65 and $C_D$ varies from 2.26 to 2.71 as the rotational axis position varies from positions C (upper 30% of the wing) to A (top of the wing). The rotational axis of our model is located within the upper 20% of the wing chord and that of real insects is located near the leading edge. As a consequence, the effect of the location of the rotational axis is negligible as long as the rotational axis is located near the top of the wing chord or the leading edge.

A convergence test in which the fluid grid is refined is also provided here. Fig. A5 shows the three fluid grids (meshes O, A and B) employed. Mesh O (the number of nodes and elements is 3417 and 6600, respectively) is used to give the results in Figs A2, A3 and A4. The refined meshes A (the number of nodes and elements is 3905 and 7560, respectively) and B (the number of nodes and elements is 4697 and 9120, respectively) have 1.4 and 2 times finer space resolutions, respectively, around the wing. As shown in Fig. A6, the force coefficients given by using these meshes show very good agreement. As a consequence, we employed mesh O throughout this study.

## REFERENCES

**Bathe, K. J. and Dvorkin, E. N.** (1985). A four-node plate bending element based on Mindlin/Reissner plate theory and a mixed interpolation. *Int. J. Numer. Methods Eng.* **21**, 367-383.
**Birch, J. M. and Dickinson, M. H.** (2003). The influence of wing-wake interactions on the production of aerodynamic forces in flapping flight. *J. Exp. Biol.* **206**, 2257-2272.
**Dickinson, M. H., Lehmann, F.-O. and Sane, P. S.** (1999). Wing rotation and the aerodynamic basis of insect flight. *Science* **284**, 1954-1960.
**Ellington, C. P.** (1984a). The aerodynamics of hovering insect flight. II. Morphological parameters. *Philos. Trans. R. Soc. Lond. B, Biol. Sci.* **305**, 17-40.
**Ellington, C. P.** (1984b). The aerodynamics of hovering insect flight. III. Kinematics. *Philos. Trans. R. Soc. Lond. B, Biol. Sci.* B **305**, 41-78.
**Ellington, C. P., Van den Berg, C., Willmott, A. P. and Thomas, L. R.** (1996). Leading-edge vortices in insect flight. *Nature* **384**, 626-630.
**Ennos, A. R.** (1987). A comparative study of the flight mechanism of Diptera. *J. Exp. Biol.* **127**, 355-372.
**Ennos, A. R.** (1988a). The importance of torsion in the design of insect wings. *J. Exp. Biol.* **140**, 137-160.
**Ennos, A. R.** (1988b). The inertial cause of wing rotation in Diptera. *J. Exp. Biol.* **140**, 161-169.
**Ennos, A. R.** (1989). Inertial and aerodynamic torques on the wings of Diptera in flight. *J. Exp. Biol.* **142**, 87-95.
**Hughes, T. J. R., Liu, W. K. and Zimmerman, T. K.** (1981). Lagrangian–Eulerian finite element formulation for incompressible viscous flows. *Comput. Meth. Appl. Mech. Eng.* **29**, 329-349.
**Ishihara, D. and Yoshimura, S.** (2005). A monolithic approach for interaction of incompressible viscous fluid and an elastic body based on fluid pressure Poisson equation. *Int. J. Numer. Methods Eng.* **64**, 167-203.
**Ishihara, D., Kanei, S., Yoshimura, S. and Horie, T.** (2008). Efficient parallel analysis of shell-fluid interaction problem by using monolithic method based on consistent pressure Poisson equation. *J. Comput. Sci. Technol.* **2**, 185-196.
**Jensen, M. and Weis-Fogh, T.** (1962). Biology and physics of locust flight. V. Strength and elasticity of locust cuticle. *Philos. Trans. R. Soc. Lond. B, Biol. Sci.* **245**, 137-169.
**Liu, H., Ellington, C. P., Kawachi, K., Van den Berg, C. and Willmott, A. P.** (1998). A computational fluid dynamic study of hawkmoth hovering. *J. Exp. Biol.* **201**, 461-477.
**Luo, G. and Sun, M.** (2005). The effects of corrugation and wing planform on the aerodynamic force production of sweeping model insect wings. *Acta Mech. Sinica.* **21**, 531-541.
**Miller, L. A. and Peskin, C. S.** (2005). A computational fluid dynamics of 'clap and fling' in the smallest insects. *J. Exp. Biol.* **208**, 195-212.
**Noguchi, H. and Hisada, T.** (1993). Sensitivity analysis in post-buckling problems of shell structure. *Comput. Struct.* **47**, 699-710.
**Ramamurti, R. and Sandberg, W. C.** (2002). A three-dimensional computational study of the aerodynamic mechanisms of insect flight. *J. Exp. Biol.* **205**, 1507-1518.
**Rugonyi, S. and Bathe, K. J.** (2001). On finite element analysis of fluid flows fully coupled with structural interactions. *Comput. Model. Eng. Sci.* **2**, 195-212.
**Sun, M. and Tang, J.** (2002). Unsteady aerodynamic force generation by a model fruit fly wing in flapping motion. *J. Exp. Biol.* **205**, 55-70.
**Tezduyar, T. E., Mital, S., Ray, S. E. and Shih, R.** (1992). Incompressible flow computations with stabilized bilinear and linear equal-order-interpolation velocity-pressure elements. *Comput. Methods Appl. Mech. Eng.* **95**, 221-242.
**Usherwood, J. R. and Ellington, C. P.** (2002). The aerodynamics of revolving wings. I. Model hawkmoth wings. *J. Exp. Biol.* **205**, 1547-1564.
**Wainwright, S. A., Biggs, W. D., Currey, J. D. and Gosline, J. M.** (1982). *Mechanical Design in Organisms*. Princeton, NJ: Princeton University Press.
**Wang, Z. J.** (2000). Vortex shedding and frequency selection in flapping flight. *J. Fluid Mech.* **410**, 323-341.
**Wang, Z. J., Birch, J. M. and Dickinson, M. J.** (2004). Unsteady forces and flows in low Reynolds number hovering flight: two-dimensional computation vs robotic wing experiments. *J. Exp. Biol.* **207**, 449-460.
**Wooton, R. J., Herbert, R. C., Young, P. G. and Evans, K. E.** (2003). Approaches to the structural modeling of insect wings. *Philos. Trans. R. Soc. B, Biol. Sci.* **358**, 1517-1587.
**Zhang, Q. and Hisada, T.** (2001). Analysis of fluid-structure interaction problems with structural buckling and large domain changes by ALE finite element method. *Comput. Methods Appl. Mech. Eng.* **190**, 6341-6357.